

# Selective Anionic Redox and Suppressed Structural Disorder Enabling High-Energy and Long-Life Li-Rich Layered-Oxide Cathode

Jinho Ahn, Jungmin Kang, Min-kyung Cho, Hyunyoung Park, Wonseok Ko, Yongseok Lee, Hyun-Soo Kim, Young Hwa Jung, Tae-Yeol Jeon, Hyungsub Kim, Won-Hee Ryu, Jihyun Hong,\* and Jongsoon Kim\*

Despite their high energy densities, Li-rich layered oxides suffer from low capacity retention and continuous voltage decay caused by the migration of transition-metal cations into the Li layers. The cation migration stabilizes oxidized oxygen anions through the decoordination of oxygen from the metal once the anions participate in the redox reaction. Structural disordering is thus considered inevitable in most Li-rich layered oxides. However, herein, a Mg-substituted Li-rich layered oxide,  $\text{Li}_{1.2}\text{Mg}_{0.2}\text{Ru}_{0.6}\text{O}_2$ , with high structural and electrochemical stability is presented. Although using both cationic and anionic redox reactions, Ru migration in  $\text{Li}_{1.2-x}\text{Mg}_{0.2}\text{Ru}_{0.6}\text{O}_2$  is thermodynamically unfavored as a result of selectively oxidized O ions, suppressed structural disordering, and the formation of short (1.75 Å) Ru=O bonds enabled within the layered framework, which effectively decoordinate the oxidized O ions. The unprecedentedly high structural stability of  $\text{Li}_{1.2}\text{Mg}_{0.2}\text{Ru}_{0.6}\text{O}_2$  leads to not only a high energy density of  $964 \text{ Wh kg}^{-1}$  but also outstanding rate capability and cycle performance. These findings demonstrate the potential of this practical strategy for the stabilization of Li-rich layered oxides even with prolonged cycling.

phase transitions to spinel-like or rocksalt-like disordered structures caused by the irreversible migration of transition-metal (TM) ions into the Li layers during long-term battery operation. The structural evolution continuously shuffles the chemical potential of Li ions and impedes Li-ion hopping, resulting in gradual voltage decay and poor cycle life.

A predominant theory of the origin of TM migration emphasizes the ability of the material to stabilize oxygen holes and inhibit oxygen release, which increases with the covalency of the TM–O bond. When using a 4d TM instead of a 3d TM, the enhanced covalency between the TM and O enables the reversible anionic redox.<sup>[2,7–9]</sup> For example,  $\text{Li}_2\text{RuO}_3$  reversibly exhibits high capacity of the cationic and anionic redox couples and releases a negligible amount of  $\text{O}_2$  gas.<sup>[10]</sup> Nevertheless, significant voltage decay is observed

for  $\text{Li}_2\text{RuO}_3$ , which stems from the accumulation of Ru cations in the Li layers,<sup>[11,12]</sup> indicating that the ability to hold oxygen in its lattice does not necessarily inhibit TM migration. Recently, Chueh and co-workers proposed a thermodynamic explanation for the coupling between the anionic redox and TM migration, which is that the oxidized oxygen anions favor less coordination with TM cations; this is achievable via structural

## 1. Introduction

The simultaneous use of cation and anionic redox reactions in Li-rich layered oxides (LRLOs) results in high energy densities ( $\approx 1100 \text{ Wh kg}^{-1}$ ) far exceeding those of conventional stoichiometric layered oxides,  $\text{LiMO}_2$  ( $\approx 800 \text{ Wh kg}^{-1}$ ), in Li-ion batteries (LIBs).<sup>[1–6]</sup> However, LRLOs generally suffer from undesired

J. Ahn, J. Kang, H. Park, W. Ko, Y. Lee, J. Kim  
Department of Energy Science  
Sungkyunkwan University  
Suwon 16419, Republic of Korea  
E-mail: jongsoonkim@skku.edu

M.-k. Cho  
Advanced Analysis Center  
Korea Institute of Science and Technology (KIST)  
14 Gil 5 Hwarang-ro, Seongbuk-gu, Seoul 02792, Republic of Korea  
H.-S. Kim, W.-H. Ryu  
Department of Chemical and Biological Engineering  
Sookmyung Women's University  
100 Cheongpa-ro 47-gil, Yongsan-gu, Seoul 04310, Republic of Korea

 The ORCID identification number(s) for the author(s) of this article can be found under <https://doi.org/10.1002/aenm.202102311>.

Y. H. Jung, T.-Y. Jeon  
Beamline Division  
Pohang Accelerator Laboratory (PAL)  
Pohang 37673, Republic of Korea

H. Kim  
Korea Atomic Energy Research Institute (KAERI)  
Daedeok-daero 989 Beon-Gil, Yuseong-gu, Daejeon 34057, Republic of Korea

J. Hong  
Energy Materials Research Center  
Korea Institute of Science and Technology (KIST)  
14 Gil 5 Hwarang-ro, Seongbuk-gu, Seoul 02792, Republic of Korea  
E-mail: jihyunh@kist.re.kr

DOI: 10.1002/aenm.202102311

disordering.<sup>[13–15]</sup> It is therefore essential to design novel LRLOs with the capability to stabilize oxidized oxygen species without significant TM migration and to hold the oxygen anions with sufficient TM–O covalency to improve the practical feasibility of  $\text{Li}_{1+x}\text{M}_{1-x}\text{O}_2$ .

Herein, we report a new Mg-substituted LRLO,  $\text{Li}_{1.2}\text{Mg}_{0.2}\text{Ru}_{0.6}\text{O}_2$  or  $\text{Li}_{2-2x}\text{Ru}_{1-x}\text{Mg}_{3x}\text{O}_3$  ( $x = 0.1$ ), with excellent capacity and voltage retention enabled by thermodynamically suppressed structural disordering. While reversibly utilizing 93% of the theoretical capacity ( $283 \text{ mAh g}^{-1}$ ), corresponding to 1.12 Li per formula unit below the low charge cut-off voltage of 4.4 V (vs  $\text{Li}^+/\text{Li}$ ) based on cationic and anionic redox reactions,  $\text{Li}_{1.2}\text{Mg}_{0.2}\text{Ru}_{0.6}\text{O}_2$  underwent the reversible change of long-range structural ordering with negligible out-of-plane and in-plane cation migration. Using combined first-principles calculations and various structural probes, we reveal that the Mg ions stabilize the neighboring Ru in octahedral sites in the delithiated state by selectively oxidizing oxygen anions and forming short (1.75 Å) Ru=O bonds through a slight distortion, which effectively decoordinates O anions from TM cations. Because of the high structural stability,  $\text{Li}_{1.2}\text{Mg}_{0.2}\text{Ru}_{0.6}\text{O}_2$  exhibits 46% less voltage decay than  $\text{Li}_2\text{RuO}_3$  and excellent cycle performance, retaining 83% of its initial capacity after 300 cycles. The suppressed cation hopping of  $\text{Li}_{1.2}\text{Mg}_{0.2}\text{Ru}_{0.6}\text{O}_2$  results in high rate capability, delivering a specific capacity of  $194 \text{ mAh g}^{-1}$  at a current density of  $608 \text{ mA g}^{-1}$ , corresponding to 68.5% of the capacity at  $15.2 \text{ mA g}^{-1}$ .

## 2. Results and Discussion

### 2.1. Comparison of Electrochemistry of $\text{Li}_{1.2}\text{Mg}_{0.2}\text{Ru}_{0.6}\text{O}_2$ and $\text{Li}_2\text{RuO}_3$

We designed  $\text{Li}_{1.2}\text{Mg}_{0.2}\text{Ru}_{0.6}\text{O}_2$  as a model system comparable to  $\text{Li}_2\text{RuO}_3$  with respect to the redox chemistry. The oxidation state of Ru is +4 in both materials in their pristine states. Theoretically,  $\text{Ru}^{4+}/\text{Ru}^{5+}$  cation oxidation results in the extraction of half of the Li ions, forming  $\text{Li}_{0.6}\text{Mg}_{0.2}\text{Ru}_{0.6}\text{O}_2$  and  $\text{Li}_1\text{Ru}^{5+}\text{O}_3$ , respectively. When fully delithiated, the formal oxidation states of oxygen are –1.7 and –1.67 in  $\text{Mg}_{0.2}\text{Ru}_{0.6}\text{O}_2$  and  $\text{RuO}_3$ , respectively. As  $\text{Mg}^{2+}$  is a redox-inactive element, we hypothesize that  $\text{Mg}^{2+}$  serves as a structural stabilizer.  $\text{Li}_{1.2}\text{Mg}_{0.2}\text{Ru}_{0.6}\text{O}_2$  was prepared via a simple solid-state method, and the detailed experimental procedure is described in the Experimental Section. As shown in Figure 1a, using X-ray diffraction (XRD) analysis and Rietveld refinement,  $\text{Li}_{1.2}\text{Mg}_{0.2}\text{Ru}_{0.6}\text{O}_2$  was characterized as a layered structure (space group: monoclinic  $C2/c$ ,  $a = 5.02059(16) \text{ \AA}$ ,  $b = 8.7517(3) \text{ \AA}$ ,  $c = 9.85575(19) \text{ \AA}$ , and  $\beta = 99.842(3)^\circ$ ) with no impurity phases. The low  $R$ -factors ( $R_p = 9.26\%$ ,  $R_1 = 4.77\%$ ,  $R_F = 3.02\%$ , and  $\chi^2 = 9.93\%$ ) indicate the high accuracy of the Rietveld refinement. The detailed structural information of  $\text{Li}_{1.2}\text{Mg}_{0.2}\text{Ru}_{0.6}\text{O}_2$ , including the atomic positions,  $B_{\text{iso}}$ , and occupancies, are tabulated in Table S1 (Supporting Information). In addition, Mg was present at the atomic sites of Ru and Li in the TM layer of the structure. The sharp superlattice peaks in the  $2\theta$  range of  $20^\circ$ – $32^\circ$  reflect the honeycomb-like in-plane structural ordering of  $\text{Li}(\text{RM})_2$  ( $\text{RM} = \text{Ru–Mg}$ ) with few antisite defects or stacking faults.<sup>[16]</sup>

The transmission electron microscope (TEM) image and energy-dispersive X-ray spectroscopy (EDS) elemental maps

(Figure 1b) reveal that Mg and Ru were homogeneously distributed in the  $\text{Li}_{1.2}\text{Mg}_{0.2}\text{Ru}_{0.6}\text{O}_2$  particles. The atomic ratio of Ru to Mg was 3.01, which is consistent with the value measured using inductively coupled plasma atomic emission spectrometry (Table S2, Supporting Information). The average particle size was  $\approx 1 \mu\text{m}$ , as observed in the field-emission scanning electron microscopy (FE-SEM) images in Figure S1 (Supporting Information). The selected-area diffraction patterns (SAED, Figure 1c) indicated the presence of the (002), (11 $\bar{1}$ ), and (113) planes of a monoclinic phase and confirmed the single-crystalline particles of the synthesized material.

To predict the electrochemical properties and reaction mechanism of  $\text{Li}_{1.2}\text{Mg}_{0.2}\text{Ru}_{0.6}\text{O}_2$  during  $\text{Li}^+$  de/intercalation, we performed first-principles calculations based on the structural information obtained from the XRD and Rietveld refinement analyses. To determine the suitable supercell structure for first-principles calculation, we prepared various  $\text{Li}_{1.2}\text{Mg}_{0.2}\text{Ru}_{0.6}\text{O}_2$  supercells with different Ru/Mg/Li arrangement using cluster-assisted statistical mechanics (CASM) software<sup>[17]</sup> and compared their formation energies using first-principles calculation. As shown in Figure S2 (Supporting Information), the supercell used in our research was the most thermodynamically stable supercell. Numerous  $\text{Li}^+/\text{vacancy}$  configurations for various  $\text{Li}_x\text{Mg}_{0.2}\text{Ru}_{0.6}\text{O}_2$  compositions were prepared using the CASM software. Their formation energies were compared to identify the thermodynamically stable crystal structures of  $\text{Li}_x\text{Mg}_{0.2}\text{Ru}_{0.6}\text{O}_2$ , and then, they were arranged using a convex-hull plot (Figure S3a, Supporting Information). The theoretical redox potentials of  $\text{Li}_x\text{Mg}_{0.2}\text{Ru}_{0.6}\text{O}_2$  during  $\text{Li}^+$  de/intercalation were calculated using the following equation

$$V = - \frac{E[\text{Li}_{x_2}\text{Mg}_{0.2}\text{Ru}_{0.6}\text{O}_2] - E[\text{Li}_{x_1}\text{Mg}_{0.2}\text{Ru}_{0.6}\text{O}_2] - (x_2 - x_1)E[\text{Li}]}{(x_2 - x_1)F} \quad (1)$$

where  $V$  is the average redox potential in the range of  $x_1 \leq x \leq x_2$ ;  $E$  represents the calculated formation energy for the most stable configurations of each  $\text{Li}_x\text{Mg}_{0.2}\text{Ru}_{0.6}\text{O}_2$  composition; and  $E[\text{Li}]$  and  $F$  are the Li metal energy and Faraday constant, respectively. The first-principles calculations results imply that  $\approx 1.2 \text{ mol Li}^+$  are reversibly de/intercalated in the  $\text{Li}_x\text{Mg}_{0.2}\text{Ru}_{0.6}\text{O}_2$  structure. Figure S3b (Supporting Information) shows that these predicted theoretical redox potentials of  $\text{Li}_{1.2}\text{Mg}_{0.2}\text{Ru}_{0.6}\text{O}_2$  during  $\text{Li}^+$  de/intercalation are consistent with the electrochemically measured galvanostatic intermittent titration technique (GITT) results in the voltage range of 2.0–4.4 V (vs  $\text{Li}^+/\text{Li}$ ).  $\text{Li}_{1.2}\text{Mg}_{0.2}\text{Ru}_{0.6}\text{O}_2$  was shown to deliver specific capacities of 299 and  $283 \text{ mAh g}^{-1}$  during the first charge and discharge, respectively, with a high Coulombic efficiency of  $\approx 94.6\%$  for the initial cycle. These values correspond to 1.18 Li and 1.12 Li per formula unit, respectively, far exceeding the redox capability of the  $\text{Ru}^{4+}/\text{Ru}^{5+}$  couple (0.6 Li per formula unit), thereby confirming the high reactivity and reversibility of both cationic ( $\text{Ru}^{4+}/\text{Ru}^{5+}$ ) and anionic ( $\text{O}^{2-}/\text{O}^{1-}$ ) redox. The low irreversible capacity and differential electrochemical mass spectroscopy (DEMS) results (Figure S4, Supporting Information) are consistent with previous DEMS results of Ru-based Li-rich layered oxides showing negligible oxygen release during cycling,<sup>[10,18,19]</sup> based on the highly covalent nature

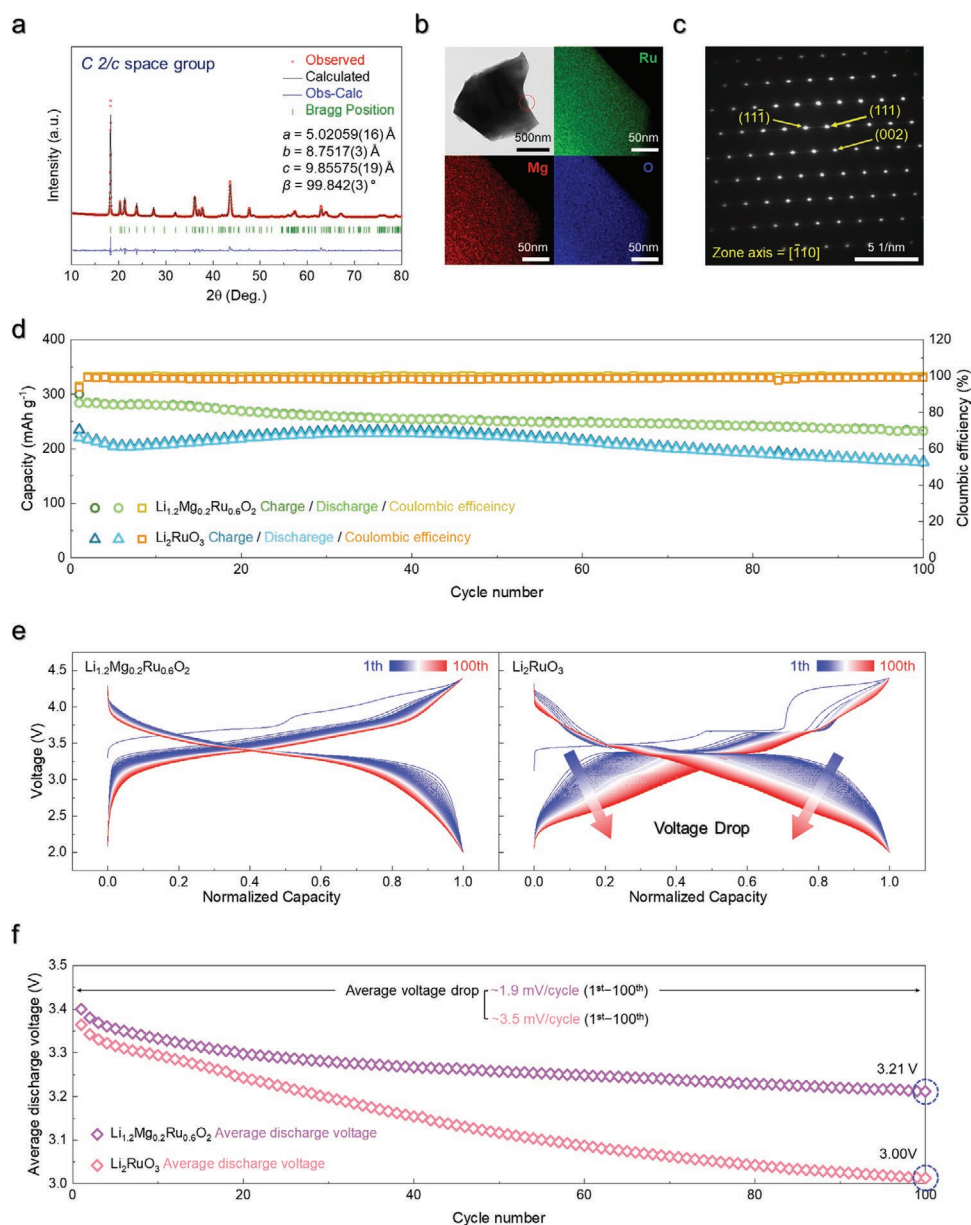


**Figure 1.** a) Rietveld refinement of XRD pattern of  $\text{Li}_{1.2}\text{Mg}_{0.2}\text{Ru}_{0.6}\text{O}_2$  ( $R_p = 9.26\%$ ,  $R_1 = 4.77\%$ ,  $R_f = 3.02\%$ ,  $\chi^2 = 9.93\%$ ). b) TEM-EDS map of  $\text{Li}_{1.2}\text{Mg}_{0.2}\text{Ru}_{0.6}\text{O}_2$  (atomic ratio of Mg:Ru = 1:3.01). c) SAED pattern. d) Comparison of charge/discharge capacities and Coulombic efficiency in  $\text{Li}_{1.2}\text{Mg}_{0.2}\text{Ru}_{0.6}\text{O}_2$  and  $\text{Li}_2\text{RuO}_3$  over 100 cycles at  $15.2 \text{ mA g}^{-1}$ . e) Comparison of normalized charge/discharge profiles for 100 cycles in  $\text{Li}_{1.2}\text{Mg}_{0.2}\text{Ru}_{0.6}\text{O}_2$  and  $\text{Li}_2\text{RuO}_3$ . f) Comparison of average discharge voltage in  $\text{Li}_{1.2}\text{Mg}_{0.2}\text{Ru}_{0.6}\text{O}_2$  and  $\text{Li}_2\text{RuO}_3$ .

of 4d transition metal–oxygen bonds. The highly accessible capacity within a reasonable voltage window (2.0–4.4 V vs Li) is consistent with the theoretical electrochemistry predicted by first-principles calculations. In addition, it was verified that  $\text{Li}_{1.2}\text{Mg}_{0.2}\text{Ru}_{0.6}\text{O}_2$  exhibited poor Coulombic efficiency of  $\approx 89.5\%$  in the voltage range of 2.0–4.8 V (vs  $\text{Li}^+/\text{Li}$ ), whereas its Coulombic efficiency was greater than  $\approx 94.6\%$  in the voltage range of 2.0–4.4 V (Figure S5, Supporting Information). The reduced Coulombic efficiency in the voltage range of 2.0–4.8 V was speculated to result from the irreversible reaction caused by the instability of conventional carbonate-based electrolytes in the high-voltage region above 4.4 V.<sup>[20–22]</sup>

We then compared the electrochemistry of  $\text{Li}_{1.2}\text{Mg}_{0.2}\text{Ru}_{0.6}\text{O}_2$  with that of  $\text{Li}_2\text{RuO}_3$  with the same space group and redox couples and similar particle morphology (Figure S6, Supporting Information). According to the initial charge and discharge measured by GITT in the voltage range of 2.0–4.4 V at a current density of  $15.2 \text{ mA g}^{-1}$ ,  $\text{Li}_{1.2}\text{Mg}_{0.2}\text{Ru}_{0.6}\text{O}_2$  exhibited a higher reversible capacity than  $\text{Li}_2\text{RuO}_3$  (Figure S7, Supporting Information). For the  $\text{Ru}^{4+}/\text{Ru}^{5+}$  redox reaction, 0.6 mol  $\text{Li}^+$  and 1 mol  $\text{Li}^+$  were deintercalated from  $\text{Li}_{1.2}\text{Mg}_{0.2}\text{Ru}_{0.6}\text{O}_2$  and  $\text{Li}_2\text{RuO}_3$ , respectively, with specific capacities of  $\approx 152$  and  $\approx 164 \text{ mAh g}^{-1}$ , respectively. Whereas there were no remarkable differences in the  $\text{Ru}^{4+}/\text{Ru}^{5+}$  redox reaction for  $\text{Li}_{1.2}\text{Mg}_{0.2}\text{Ru}_{0.6}\text{O}_2$

and  $\text{Li}_2\text{RuO}_3$ , the anionic redox reactions of  $\text{O}^{2-}/\text{O}^{1-}$  differed for  $\text{Li}_{1.2}\text{Mg}_{0.2}\text{Ru}_{0.6}\text{O}_2$  and  $\text{Li}_2\text{RuO}_3$ . For  $\text{Li}_2\text{RuO}_3$ , the voltage greatly increased after 1 mol Li deintercalation, and only 0.4 mol  $\text{Li}^+$  (corresponding to  $\approx 65.6 \text{ mAh g}^{-1}$ ) could be deintercalated from the structure via the anionic redox reactions of  $\text{O}^{2-}/\text{O}^{1-}$ . In contrast, for  $\text{Li}_{1.2}\text{Mg}_{0.2}\text{Ru}_{0.6}\text{O}_2$ , 0.58 mol  $\text{Li}^+$  (corresponding to  $\approx 146.9 \text{ mAh g}^{-1}$ ) could be deintercalated by the anionic redox reactions of  $\text{O}^{2-}/\text{O}^{1-}$  without remarkable change of the voltage profile. The increased use of the anionic redox reaction (0.6Li/2O vs 0.4Li/3O) is attributed to the improved structural stability of  $\text{Li}_{1.2}\text{Mg}_{0.2}\text{Ru}_{0.6}\text{O}_2$ , which enabled occurrence of the stable and considerable anionic redox reactions of  $\text{O}^{2-}/\text{O}^{1-}$  at  $\text{Li}_{1.2}\text{Mg}_{0.2}\text{Ru}_{0.6}\text{O}_2$  unlike for  $\text{Li}_2\text{RuO}_3$ . Because of the different phase behavior during charge/discharge, the voltage plateau of anionic redox reaction appeared at lower potential for  $\text{Li}_{1.2}\text{Mg}_{0.2}\text{Ru}_{0.6}\text{O}_2$  than for  $\text{Li}_2\text{RuO}_3$ . The long-term electrochemical stability of  $\text{Li}_{1.2}\text{Mg}_{0.2}\text{Ru}_{0.6}\text{O}_2$  was then measured and compared with  $\text{Li}_2\text{RuO}_3$ . Figure 1d confirms that  $\text{Li}_{1.2}\text{Mg}_{0.2}\text{Ru}_{0.6}\text{O}_2$  and  $\text{Li}_2\text{RuO}_3$  both exhibited stable cycle performance, retaining specific capacities of 232 and 174  $\text{mAh g}^{-1}$  after 100 cycles, respectively, with high Coulombic efficiencies above 99% in both cases. Interestingly, we note that the evolution of the voltage profiles significantly differed (Figure 1e). The electrochemical profiles of  $\text{Li}_{1.2}\text{Mg}_{0.2}\text{Ru}_{0.6}\text{O}_2$  stably retained their overall shape for 100 cycles, whereas  $\text{Li}_2\text{RuO}_3$  suffered from dramatic voltage decay, losing its original profile, as observed in the differential capacity versus voltage ( $dQ/dV$ ) plots (Figure S8, Supporting Information). In addition, we calculated the average discharge voltages by dividing the total energy density by the specific capacity measured in the voltage range of 2.0–4.4 V (vs  $\text{Li}^+/\text{Li}$ ). Quantitatively, the average discharge voltages of  $\text{Li}_{1.2}\text{Mg}_{0.2}\text{Ru}_{0.6}\text{O}_2$  and  $\text{Li}_2\text{RuO}_3$  decreased from 3.40 to 3.21 V and from 3.36 to 3.00 V, respectively, from the 1st to 100th cycle (Figure 1f). For  $\text{Li}_{1.2}\text{Mg}_{0.2}\text{Ru}_{0.6}\text{O}_2$ , the rate of voltage decay was  $-1.9 \text{ mV per cycle}$ , equivalent to 54% of that for  $\text{Li}_2\text{RuO}_3$ . As the chemical potential of Li ions, i.e., the local atomic configuration, determines the (de)lithiation voltage, we attribute the suppressed voltage decay observed in  $\text{Li}_{1.2}\text{Mg}_{0.2}\text{Ru}_{0.6}\text{O}_2$  to the mitigated cation migration. In contrast,  $\text{Li}_2\text{RuO}_3$  suffers from structural disordering, similar to most LRLOs.<sup>[11,15,23,24]</sup>

## 2.2. High Structural Stability of $\text{Li}_{1.2}\text{Mg}_{0.2}\text{Ru}_{0.6}\text{O}_2$ with Suppressed Structural Disordering and Restricted Cation Migration

To confirm the role of Mg in stabilizing the  $\text{Li}_{1.2}\text{Mg}_{0.2}\text{Ru}_{0.6}\text{O}_2$  structure, we captured scanning transmission electron microscopy-high-angle annular dark field (STEM-HAADF) images and selected-area electron diffraction (SAED) patterns of  $\text{Li}_{1.2}\text{Mg}_{0.2}\text{Ru}_{0.6}\text{O}_2$  and  $\text{Li}_2\text{RuO}_3$  electrodes before and after repeating charge and discharge for 50 cycles (Figure 2a–d). In the pristine states, both materials are consisted of layered structures without interlayer cation mixing (Figure 2a,c), with histograms across the Li and RM slabs (RM = Ru–Mg) confirming a sharp intensity contrast between the Li and RM layers. STEM-HAADF analyses further showed that Mg was not detected in the Li layer of the  $\text{Li}_{1.2}\text{Mg}_{0.2}\text{Ru}_{0.6}\text{O}_2$  structure. After 50 cycles,  $\text{Li}_{1.2}\text{Mg}_{0.2}\text{Ru}_{0.6}\text{O}_2$  and  $\text{Li}_2\text{RuO}_3$  exhibited distinct structural characteristics. Notably,  $\text{Li}_{1.2}\text{Mg}_{0.2}\text{Ru}_{0.6}\text{O}_2$  maintained

its original layered structure with a negligible number of heavy elements in the Li layers (Figure 2b). Accordingly, no notable differences were observed in the SAED patterns of the pristine and cycled samples. This high structural stability is considered to be the origin of the suppressed voltage decay (Figure 1e) of  $\text{Li}_{1.2}\text{Mg}_{0.2}\text{Ru}_{0.6}\text{O}_2$ . In stark contrast, severe disordering of the original structure of  $\text{Li}_2\text{RuO}_3$  occurred during prolonged cycling (Figure 2d), consistent with previous reports.<sup>[25]</sup> The STEM-HAADF image reveals a considerable number of Ru ions in the octahedral sites of the Li layer, as highlighted by the red arrows in the signal profiles. The SAED pattern reveals the emergence of additional spots, indicating the local formation of new phases. Moreover, to improve the validity of our observation, we included more STEM-HAADF images of cycled samples in Figure S9 (Supporting Information). Ex situ XRD analysis confirmed the extraordinary structural stability of  $\text{Li}_{1.2}\text{Mg}_{0.2}\text{Ru}_{0.6}\text{O}_2$ . The honeycomb-like in-plane cation ordering remained intact even after long-term cycling (Figure S10, Supporting Information), which has rarely been observed in most LRLOs exploiting anionic redox.<sup>[15,26,27]</sup>

Because the long-term structural evolution is determined by the accumulation of the irreversibility in every cycle, we investigated the phase behavior of  $\text{Li}_{1.2}\text{Mg}_{0.2}\text{Ru}_{0.6}\text{O}_2$  and  $\text{Li}_2\text{RuO}_3$  during the initial delithiation and lithiation processes using operando XRD analysis (Figure 2e–h). The XRD patterns of  $\text{Li}_{1.2}\text{Mg}_{0.2}\text{Ru}_{0.6}\text{O}_2$  (Figure 2e,f) confirm its unprecedentedly high structural stability and reversibility. As shown in Figure S11 (Supporting Information), the (002) peak shifted toward lower angle during  $\text{Ru}^{4+}/\text{Ru}^{5+}$  oxidation and the formation of  $\text{Li}_{0.6}\text{Mg}_{0.2}\text{Ru}_{0.6}\text{O}_2$ . This result indicates the occurrence of a solid-solution reaction with lattice expansion of 0.1% along the *c*-axis (from 9.89 to 9.91 Å). Further charging beyond 3.8 to 4.1 V and oxidizing oxygen anions resulted in a transition from the  $\alpha$  phase (O3-type phase) to the  $\alpha'$  phase (distorted O3-type phase). At the voltage plateau at 4.1 V, the delithiation occurred via a solid-solution reaction of the  $\alpha'$  phase, resulting in an increase in the *c* lattice parameter by 0.01%. The total volume change in  $\text{Li}_{1.2}\text{Mg}_{0.2}\text{Ru}_{0.6}\text{O}_2$  was less than 3%. During discharge, the phase transition occurred symmetrically in a reverse manner, resulting in full recovery of the original structure. Notably, the intensity and sharpness of the superstructure peaks and (002) peak were maintained throughout the electrochemical cycling (Figure S12, Supporting Information). These results strongly indicate that the migration of Mg and Ru cations did not occur in either the in-plane or out-of-plane directions in  $\text{Li}_{1.2}\text{Mg}_{0.2}\text{Ru}_{0.6}\text{O}_2$  (Figure S13 and Tables S3–S5, Supporting Information). In contrast,  $\text{Li}_2\text{RuO}_3$  underwent a phase transition from the  $\alpha$  to  $\beta$  phase (O1-type phase) accompanying the irreversible cation migration, similar to other LRLOs.<sup>[8,11,15,27–29]</sup> Notably, the  $\alpha'$  phase of  $\text{Li}_{1.2-x}\text{Mg}_{0.2}\text{Ru}_{0.6}\text{O}_2$  does not require slab sliding to form, unlike the  $\beta$  phase of  $\text{Li}_{2-x}\text{RuO}_3$ . Slab sliding causes severe strain or micro-cracks of the particles. The higher structural stability of  $\text{Li}_{1.2}\text{Mg}_{0.2}\text{Ru}_{0.6}\text{O}_2$  during  $\text{Li}^+$  de/intercalation relative to that of  $\text{Li}_2\text{RuO}_3$  was also confirmed by comparing the variation of the residual strain as a function of Li content for  $\text{Li}_{1.2}\text{Mg}_{0.2}\text{Ru}_{0.6}\text{O}_2$  and  $\text{Li}_2\text{RuO}_3$ . We calculated the lattice strain using the Williamson–Hall isotropic strain model (W-H ISM), based on the broadness of the operando XRD peaks.<sup>[30,31]</sup> To account for peak broadening by the

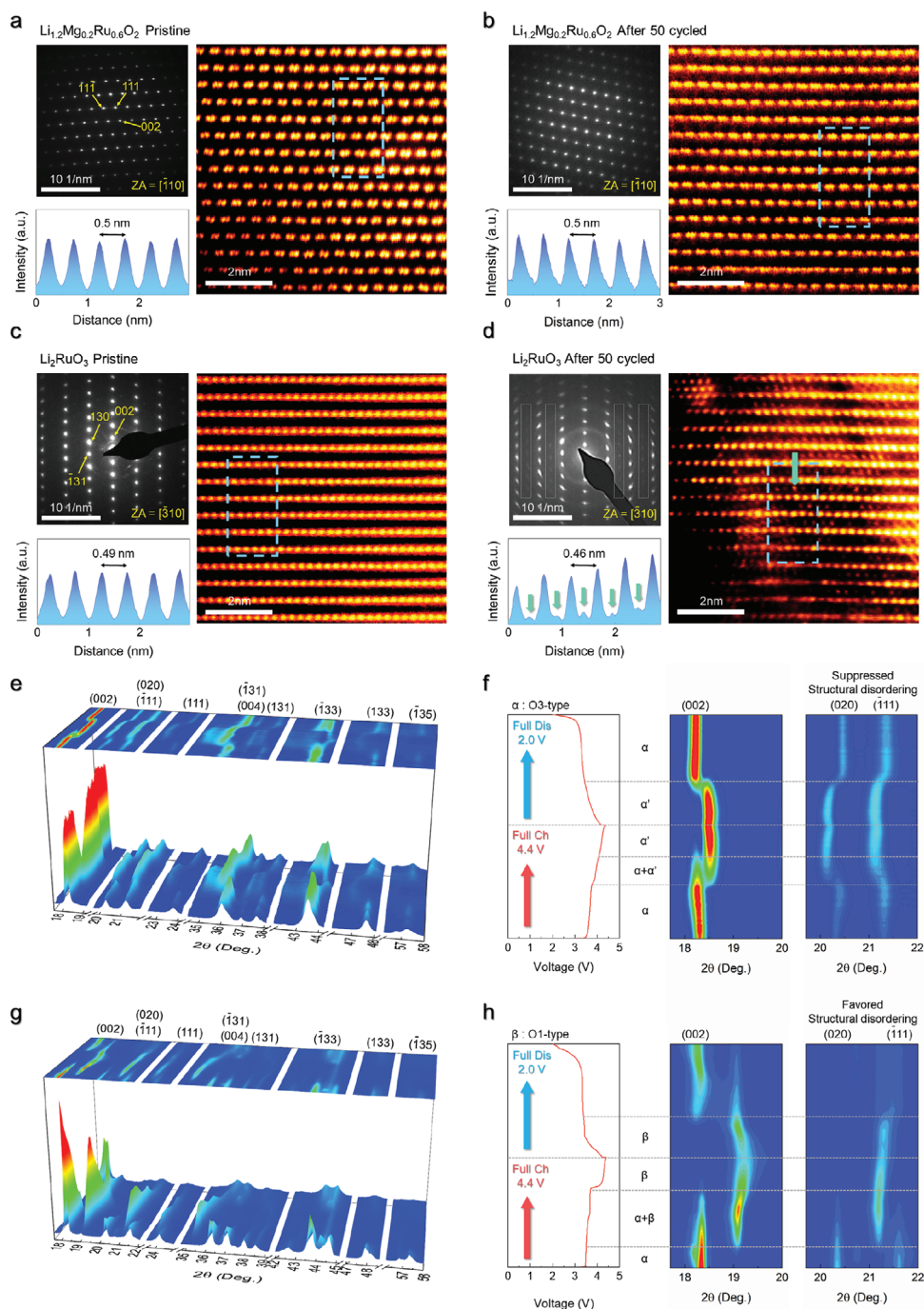


**Figure 2.** STEM-HAADF images and SAED patterns. The plots below show the HAADF signal profiles of the regions enclosed by the dotted lines in the STEM images. a)  $\text{Li}_{1.2}\text{Mg}_{0.2}\text{Ru}_{0.6}\text{O}_2$ , pristine, b)  $\text{Li}_{1.2}\text{Mg}_{0.2}\text{Ru}_{0.6}\text{O}_2$ , after 50 cycles, c)  $\text{Li}_2\text{RuO}_3$ , pristine, and d)  $\text{Li}_2\text{RuO}_3$ , after 50 cycles; images along the  $[\bar{1}10]$  and  $[\bar{3}10]$  zone axis. The highlights in the signal profiles, SAED patterns, and STEM image indicate the Ru migration. e) Operando XRD patterns and f) magnified views of  $\text{Li}_{1.2}\text{Mg}_{0.2}\text{Ru}_{0.6}\text{O}_2$  during charge/discharge. g) Operando XRD patterns and h) magnified views of  $\text{Li}_2\text{RuO}_3$  during charge/discharge.

instrumental effect, the corrected full-width at half-maximum (FWHM) was determined using the following equation

$$\beta_{\text{hkl}} = \sqrt{\beta_1^2 - \beta_2^2} \quad (2)$$

where  $\beta_{\text{hkl}}$ ,  $\beta_1$ , and  $\beta_2$  are the corrected FWHM, observed FWHM, and instrumental broadening, respectively. They were determined using lanthanum hexaboride ( $\text{LaB}_6$ ) standard

powder.<sup>[32]</sup>  $\beta_{\text{hkl}}$  indicates the contribution of lattice strain and crystallite size in the W-H ISM. The two independent factors, the lattice strain and crystallite size, also contribute to the total peak broadening, as shown in the following equation

$$\beta_{\text{hkl}} \cos \theta_{\text{hkl}} = 4\varepsilon \sin \theta_{\text{hkl}} + \frac{K\lambda}{D} \quad (3)$$

here  $\theta_{hkl}$ ,  $K$ ,  $\lambda$ , and  $\varepsilon$  are the Bragg angle, shape factor ( $=0.9$ ), X-ray wavelength, and lattice strain, respectively. The strain information can be calculated in the linear fitting with an  $x$ -axis ( $4\sin\theta_{hkl}$ ) and  $y$ -axis ( $\beta_{hkl}\cos\theta_{hkl}$ ) based on the equation above. After being charged and discharged, the lattice strain of  $\text{Li}_{1.2}\text{Mg}_{0.2}\text{Ru}_{0.6}\text{O}_2$  increased to 111.7% and recovered to 106.6% of the original value. For  $\text{Li}_2\text{RuO}_3$ , the lattice strain increased to 212.2% and 225.6% after charge and discharge, respectively, and did not recover (Figures S14 and S15, Supporting Information).  $\text{Li}_{1.2}\text{Mg}_{0.2}\text{Ru}_{0.6}\text{O}_2$  delivered a lower strain change than  $\text{Li}_2\text{RuO}_3$ , with the lack of slab sliding contributing to the high structural stability of  $\text{Li}_{1.2}\text{Mg}_{0.2}\text{Ru}_{0.6}\text{O}_2$ .

### 2.3. Localized Oxidation of Oxygen Anions in $\text{Li}_{1.2-x}\text{Mg}_{0.2}\text{Ru}_{0.6}\text{O}_2$

The reversible cationic and anionic redox reactions in  $\text{Li}_{1.2}\text{Mg}_{0.2}\text{Ru}_{0.6}\text{O}_2$  were verified by ex situ X-ray absorption near edge structure (XANES) and soft X-ray absorption spectroscopy (sXAS). The Ru K-edge XANES spectra shifted to higher energy during the initial charge to 3.9 V and negligibly moved upon further delithiation to 4.4 V (Figure 3a), indicating the sequential oxidation of Ru and O. The extended X-ray absorption fine structure (EXAFS) spectra reveal the reversible shortening and recovery of Ru–O bond lengths, confirming the reversible cationic and anionic redox reactions (Figure 3b). The successive oxidations of Ru and O during delithiation were confirmed by the sXAS O K-edge spectra and corresponding difference plots (Figure 3c). The pre-edge peak corresponds to the unoccupied Ru 4d–O 2p  $t_{2g}$  hybridized orbital moved from 530 to 529 eV, and the increased intensity during the half-charge to 3.9 V indicates an increase in the hole occupancy in the hybridized orbital, confirming the oxidation of  $\text{Ru}^{4+}$  to  $\text{Ru}^{5+}$ .<sup>[33–35]</sup> During further delithiation from 3.9 to 4.4 V, an increase in the absorbance at 530.4 eV was observed in the difference plot (lower panel of Figure 3c). The increased intensity at 530.4 eV originates from the localized feature of the oxidized oxygen state, which confirms the anion redox.<sup>[13–15,36–39]</sup>

To investigate the redox mechanism of  $\text{Li}_{1.2}\text{Mg}_{0.2}\text{Ru}_{0.6}\text{O}_2$  at the atomic level, density functional theory (DFT) calculations were performed. Figure 3d shows the changes in the projected density of states (pDOS) of O and Ru in  $\text{Li}_{1.2-x}\text{Mg}_{0.2}\text{Ru}_{0.6}\text{O}_2$ , where  $x = 0, 0.6, \text{ and } 1.2$ . The delithiation from  $\text{Li}_{1.2}\text{Mg}_{0.2}\text{Ru}_{0.6}\text{O}_2$  to  $\text{Li}_{0.6}\text{Mg}_{0.2}\text{Ru}_{0.6}\text{O}_2$  creates holes in the Ru 4d–O 2p hybrid orbital, indicating the oxidation of  $\text{Ru}^{4+}$  to  $\text{Ru}^{5+}$ , consistent with the XANES and sXAS results. The electron density in O 2p was dominant over that in Ru 4d near the Fermi level in  $\text{Li}_{0.6}\text{Mg}_{0.2}\text{Ru}_{0.6}\text{O}_2$ , indicating that the oxygen–redox reaction will likely occur during the further delithiation from  $\text{Li}_{0.6}\text{Mg}_{0.2}\text{Ru}_{0.6}\text{O}_2$ . As expected, an increased hole density in O 2p near the Fermi level was observed in  $\text{Li}_0\text{Mg}_{0.2}\text{Ru}_{0.6}\text{O}_2$ , confirming the anionic redox. The sequential oxidation of Ru and O species was further supported by the successive changes of the total magnetic moments of Ru and O, as shown in Figure S16 (Supporting Information).

Visualization of the electron and hole densities further revealed the redox mechanism of individual atoms in  $\text{Li}_{1.2-x}\text{Mg}_{0.2}\text{Ru}_{0.6}\text{O}_2$  (Figure 3e). The shape of the unoccupied Ru orbitals in  $\text{Li}_{0.6}\text{Mg}_{0.2}\text{Ru}_{0.6}\text{O}_2$  was the same as that

in  $\text{Li}_0\text{Mg}_{0.2}\text{Ru}_{0.6}\text{O}_2$ , indicating that further oxidation of Ru beyond the pentavalent state did not occur. In addition, the hole density of oxygen anions increased during the delithiation from  $\text{Li}_{0.6}\text{Mg}_{0.2}\text{Ru}_{0.6}\text{O}_2$  to  $\text{Li}_0\text{Mg}_{0.2}\text{Ru}_{0.6}\text{O}_2$ . Interestingly, in  $\text{Li}_{1.2-x}\text{Mg}_{0.2}\text{Ru}_{0.6}\text{O}_2$ , only a fraction of the oxygen anions participate in the redox reaction, whereas all the oxygen anions equally contribute to the capacity in  $\text{Li}_{2-x}\text{RuO}_3$ . For instance, the oxygen anions neighboring two Ru cations form a localized hole more than those neighboring Mg cations highlighted by dotted circles in Figure 3e. The localized oxidation of oxygen anions is attributed to the diverse local environments in  $\text{Li}_{1.2}\text{Mg}_{0.2}\text{Ru}_{0.6}\text{O}_2$  in contrast to the uniform oxygen environments in  $\text{Li}_2\text{RuO}_3$  (see Figure S17 for further details, Supporting Information). Whereas there is only one local environment of all O anions in the  $\text{Li}_{2-x}\text{RuO}_3$  structure (two Ru near each O), O anions in  $\text{Li}_{1.2-x}\text{Mg}_{0.2}\text{Ru}_{0.6}\text{O}_2$  can have various local environments because of the presence of Mg (Figure S17, Supporting Information). The possible local environments of O anions in the  $\text{Li}_{1.2-x}\text{Mg}_{0.2}\text{Ru}_{0.6}\text{O}_2$  structure are as follows: 1) two Ru near one O, 2) two Ru and one Mg near one O, 3) one Ru and one Mg near one O, and 4) one Ru and two Mg near one O. The anionic redox reaction of  $\text{O}^{2-}/\text{O}^{1-}$  can occur at the O anions with the large pDOS of the O 2p orbital below the Fermi level.<sup>[40]</sup> For the  $\text{Li}_{1.2}\text{Mg}_{0.2}\text{Ru}_{0.6}\text{O}_2$  structure, certain O anions were shown to have a large pDOS below the Fermi level, implying that certain O anions in the  $\text{Li}_{1.2}\text{Mg}_{0.2}\text{Ru}_{0.6}\text{O}_2$  structure selectively participate in the anionic redox reaction of  $\text{O}^{2-}/\text{O}^{1-}$ .

### 2.4. Origin of Suppressed Structural Disordering in Delithiated $\text{Li}_{1.2-x}\text{Mg}_{0.2}\text{Ru}_{0.6}\text{O}_2$

Given the localized oxygen oxidation induced by the Mg cations, first-principles calculations were performed to determine the thermodynamic reason for the suppressed structural disordering in the delithiated  $\text{Li}_{1.2-x}\text{Mg}_{0.2}\text{Ru}_{0.6}\text{O}_2$ . Figure 4a,b shows the site energy on the path of cation migration from the original octahedral site in RM layers to the octahedral site in Li layers. Unexpectedly, the results indicate that both the intermediate and final sites were less stable than the original site for the Ru cation in delithiated  $\text{Li}_{1.2-x}\text{Mg}_{0.2}\text{Ru}_{0.6}\text{O}_2$ , unlike for  $\text{Li}_{2-x}\text{RuO}_3$ .

We believe that the selective oxidation of oxygen anions caused by the Mg substitution contributes to the improved structural stability of the LRLO. The localized anion oxidation left some oxygen anions inert, stabilizing the (RM) $\text{O}_6$  octahedral sites. Figure 4c shows the changes in the volume of  $\text{RuO}_6$  octahedral sites in  $\text{Li}_{1.2-x}\text{Mg}_{0.2}\text{Ru}_{0.6}\text{O}_2$  and  $\text{Li}_{2-x}\text{RuO}_3$ , for which Ru and O are in comparable formal oxidation states. In the pristine states with  $\text{Ru}^{4+}$  and the half-charged states with Ru oxidized to 5+, both materials have similarly sized  $\text{RuO}_6$  octahedrons. However, when fully delithiated via anionic redox, many of the  $\text{RuO}_6$  in  $\text{Li}_{1.2-x}\text{Mg}_{0.2}\text{Ru}_{0.6}\text{O}_2$  remain more spacious than those in  $\text{Li}_{2-x}\text{RuO}_3$ . The localized oxygen oxidation and consequently mitigated contraction of the octahedral sites result in the suppressed formation of O–O dimers and, thereby, the less distorted  $\text{RuO}_6$  in  $\text{Li}_{1.2-x}\text{Mg}_{0.2}\text{Ru}_{0.6}\text{O}_2$  (Figure S18, Supporting Information). The bulky  $\text{MgO}_6$  with rigid O–Mg–O bond angles likely reduced the contraction of  $\text{RuO}_6$ . The suppressed distortion and the sufficiently large

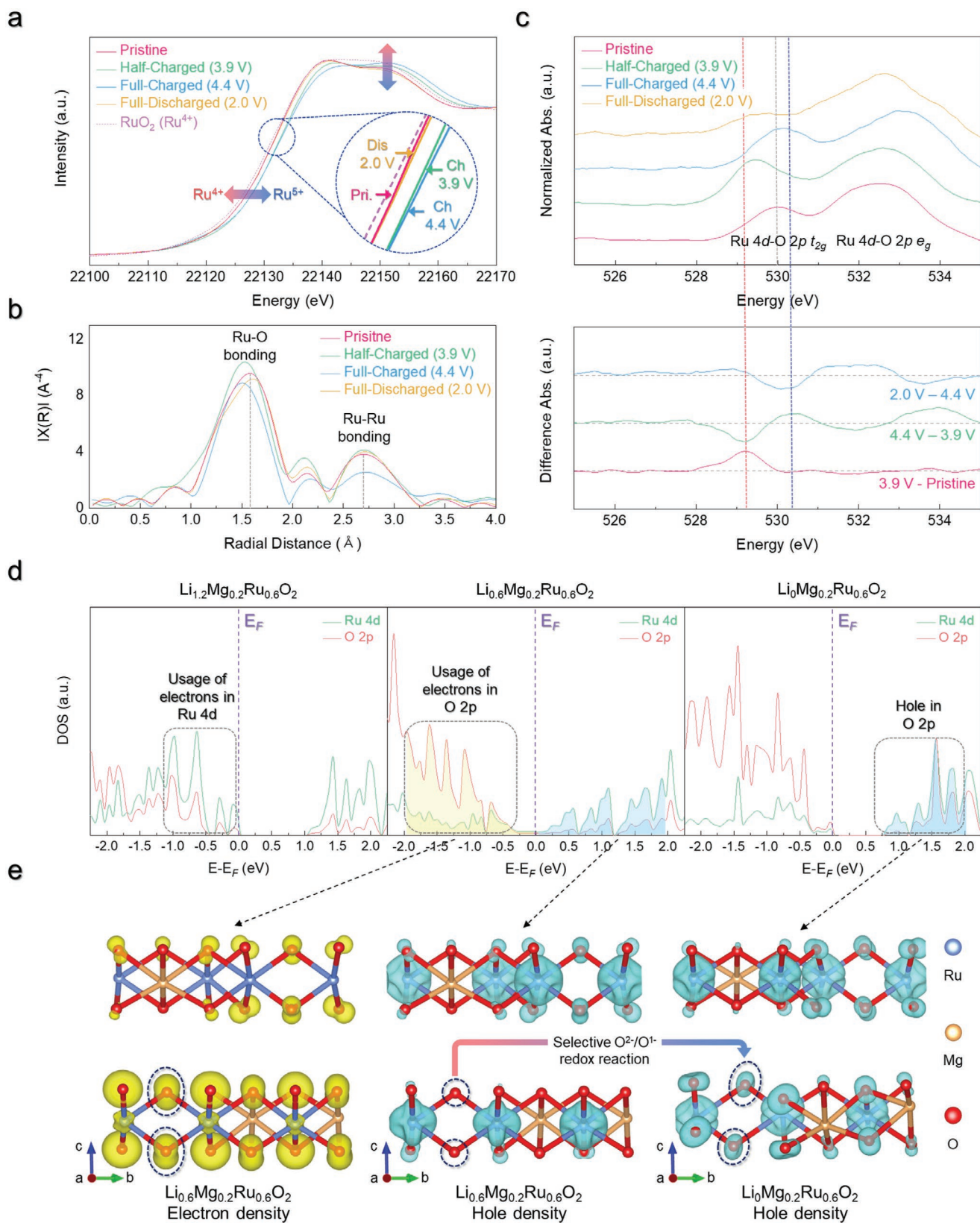


**Figure 3.** Ex situ analyses of Li<sub>1.2</sub>Mg<sub>0.2</sub>Ru<sub>0.6</sub>O<sub>2</sub>: a) Ru K-edge XANES spectra, b) EXAFS spectra, c) O K-edge sXAS spectra and difference spectra (lower panel) of sXAS obtained from (a). d) pDOS of Ru 4d and O 2p of Li<sub>x</sub>Mg<sub>0.2</sub>Ru<sub>0.6</sub>O<sub>2</sub> (0 ≤ x ≤ 1.2). e) Visualized pDOS on O 2p and Ru 4d orbitals on Li<sub>0.6</sub>Mg<sub>0.2</sub>Ru<sub>0.6</sub>O<sub>2</sub> and Li<sub>0</sub>Mg<sub>0.2</sub>Ru<sub>0.6</sub>O<sub>2</sub>: electron density (yellow) and hole density (blue).

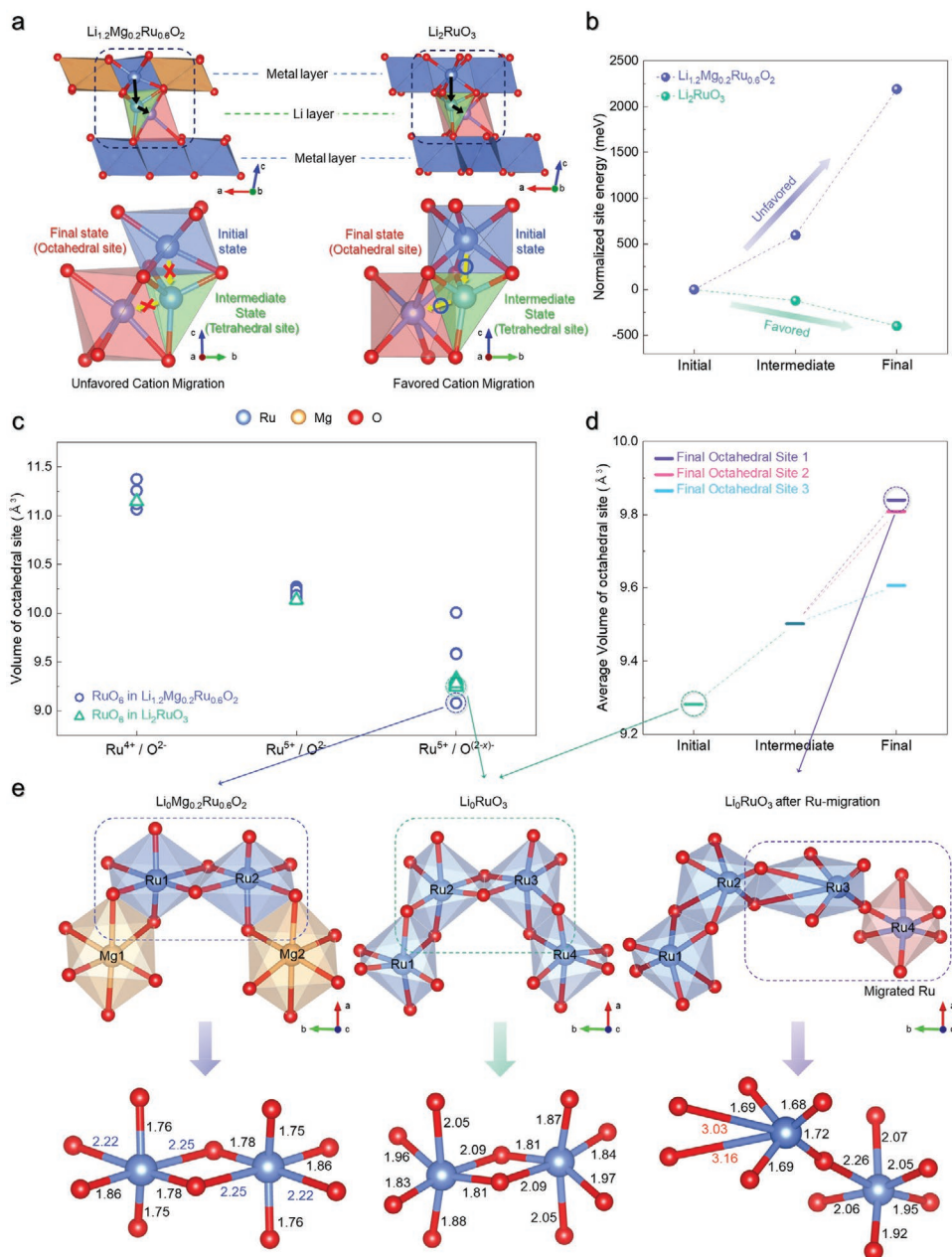


**Figure 4.** a) Illustration of Ru-migration paths from initial to intermediate to final state. b) Relative site energies of tetrahedral (intermediate state) and octahedral (final state) sites calculated along the migration path of Ru ions. The site energies were normalized based on the initial state. c) Volume of  $\text{RuO}_6$  octahedral sites in  $\text{Li}_x\text{Mg}_{0.2}\text{Ru}_{0.6}\text{O}_2$  ( $0 \leq x \leq 1.2$ ) and  $\text{Li}_x\text{RuO}_3$  ( $0 \leq x \leq 2$ ) as a function of the oxidation states of Ru and O ions. d) Average volume of  $\text{RuO}_6$  octahedral sites in  $\text{Li}_0\text{RuO}_3$  as a function of the octahedral sites of the final state. e) Magnified view of crystal structures corresponding to dotted circle and  $\text{RuO}_6$  local structure with Ru–O bond lengths in  $\text{Li}_0\text{Mg}_{0.2}\text{Ru}_{0.6}\text{O}_2$ ,  $\text{Li}_0\text{RuO}_3$ , and  $\text{Li}_0\text{RuO}_3$  after Ru-migration state.

space for  $\text{Ru}^{5+}$  stabilized the original octahedral sites in the Ru–Mg layers, making the cation migration less favorable in  $\text{Li}_{1.2-x}\text{Mg}_{0.2}\text{Ru}_{0.6}\text{O}_2$ .

For  $\text{Li}_{2-x}\text{RuO}_3$ , the severe distortion and contraction of  $\text{RuO}_6$  destabilized the original sites, inducing the thermodynamically driven Ru migration. This migration leads to the formation of short Ru=O double bonds (1.68–1.69  $\text{\AA}$ ) or makes the oxygen effectively less coordinated (e.g., Ru–O > 3.0  $\text{\AA}$  in the final state in Figure 4d,e) to stabilize the oxidized oxygen species,

consistent with a previous report.<sup>[14]</sup> Depending on the local configuration, some of the  $\text{RuO}_6$  sites in  $\text{Li}_{1.2-x}\text{Mg}_{0.2}\text{Ru}_{0.6}\text{O}_2$  have smaller volumes than those in  $\text{Li}_{2-x}\text{RuO}_3$  (highlighted in Figure 4c). The smallest  $\text{RuO}_6$  octahedrons in  $\text{Li}_0\text{Mg}_{0.2}\text{Ru}_{0.6}\text{O}_2$  consist of long Ru–O bonds (2.22–2.25  $\text{\AA}$ ), regular Ru–O bonds (1.86  $\text{\AA}$ ), and short Ru–O bonds (1.75–1.78  $\text{\AA}$ ) similar to Ru=O double bonds, showing higher heterogeneity in bond lengths than that found in  $\text{Li}_0\text{RuO}_3$  without disordering (1.81–2.09  $\text{\AA}$  in Figure 4e). The formation of effective dangling bonds and the

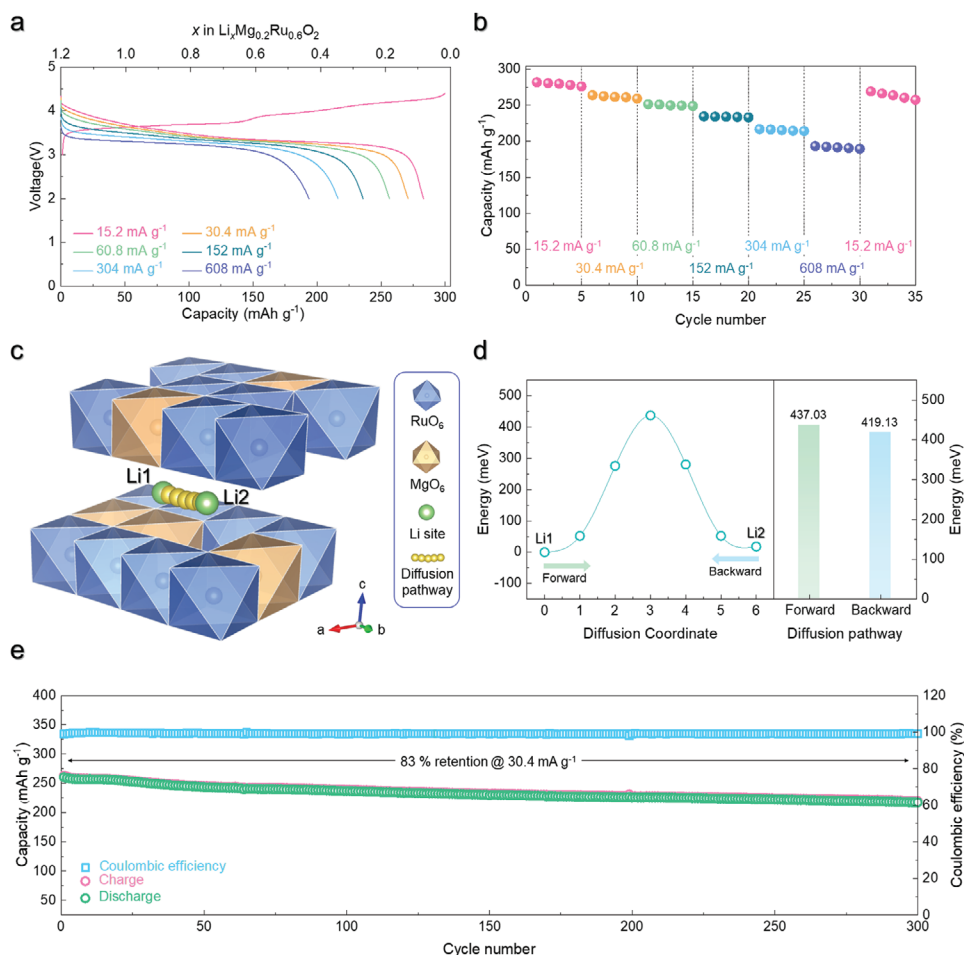


**Figure 5.** a) Charge/discharge curves of  $\text{Li}_{1.2}\text{Mg}_{0.2}\text{Ru}_{0.6}\text{O}_2$  in the voltage range of 2.0–4.4 V at various discharge current densities and a charge current density of  $15.2 \text{ mA g}^{-1}$ . b) Rate capability of  $\text{Li}_{1.2}\text{Mg}_{0.2}\text{Ru}_{0.6}\text{O}_2$ . c) Predicted  $\text{Li}^+$  diffusion pathway in  $\text{Li}_{1.2}\text{Mg}_{0.2}\text{Ru}_{0.6}\text{O}_2$  and d) predicted activation barrier energy for  $\text{Li}^+$  diffusion in  $\text{Li}_{1.2}\text{Mg}_{0.2}\text{Ru}_{0.6}\text{O}_2$ . e) Cycle performance of  $\text{Li}_{1.2}\text{Mg}_{0.2}\text{Ru}_{0.6}\text{O}_2$  at  $30.4 \text{ mA g}^{-1}$  over 300 cycles in the voltage range of 2.0–4.4 V (vs  $\text{Li}^+/\text{Li}$ ).

short bonds was enabled by a small displacement of Ru from the center of the octahedral sites without the long migration to the adjacent sites. We attribute this finding to the large honeycomb-like superstructure containing  $\text{Mg}^{2+}$ , which provides enough space for  $\text{Ru}^{5+}$  to stabilize the oxidized anions within the original sites (Figure S19, Supporting Information). The results suggest that the substitution of elements with large ionic sizes and rigid O–M–O bond angles can improve the structural stability of LRLOs.

## 2.5. Outstanding Electrochemical Performance of $\text{Li}_{1.2}\text{Mg}_{0.2}\text{Ru}_{0.6}\text{O}_2$

The in-plane and out-of-plane cation migrations of LRLOs are sluggish and partially reversible processes, impeding (de)lithiation.<sup>[41]</sup> Thus, the restriction of cation migration likely results in the high rate capability of  $\text{Li}_{1.2}\text{Mg}_{0.2}\text{Ru}_{0.6}\text{O}_2$ . Figure 5a,b shows that  $\text{Li}_{1.2}\text{Mg}_{0.2}\text{Ru}_{0.6}\text{O}_2$  delivers a specific capacity of  $194 \text{ mAh g}^{-1}$  at  $608 \text{ mA g}^{-1}$ , corresponding to 68.5% of that

measured at  $15.2 \text{ mA g}^{-1}$ . In addition to the suppressed structural disordering, we attribute the excellent rate capability to the minimized strain induced during the electrochemical cycling. As a result, Li ions can rapidly move through the unstrained paths within the crystal structure. The reduced strain of  $\text{Li}_{1.2}\text{Mg}_{0.2}\text{Ru}_{0.6}\text{O}_2$  compared with that for other LRLOs such as  $\text{Li}_2\text{RuO}_3$  (Figures S14 and S15, Supporting Information) stems from the distinct structural features. First,  $\text{Li}_{1.2-x}\text{Mg}_{0.2}\text{Ru}_{0.6}\text{O}_2$  remains in the O3 structure even in the fully delithiated state and does not form the O1 phase. The O3–O1 phase transition observed in most LRLOs<sup>[8,42,43]</sup> accompanies the sliding of the entire TM slabs along the ab-plane (Figure S20, Supporting Information). During the repeated O3–O1 and O1–O3 phase transitions, the accumulated stacking faults build up the strain within the active particle and decrease the crystallinity near the Li diffusion paths, impeding the Li migration. Second, the absence of high-valent Ru ions in the Li layers keeps the distance between the RM layers sufficiently large for the Li ions to move throughout the entire reaction. Based on the structural solution obtained experimentally, we also measured the

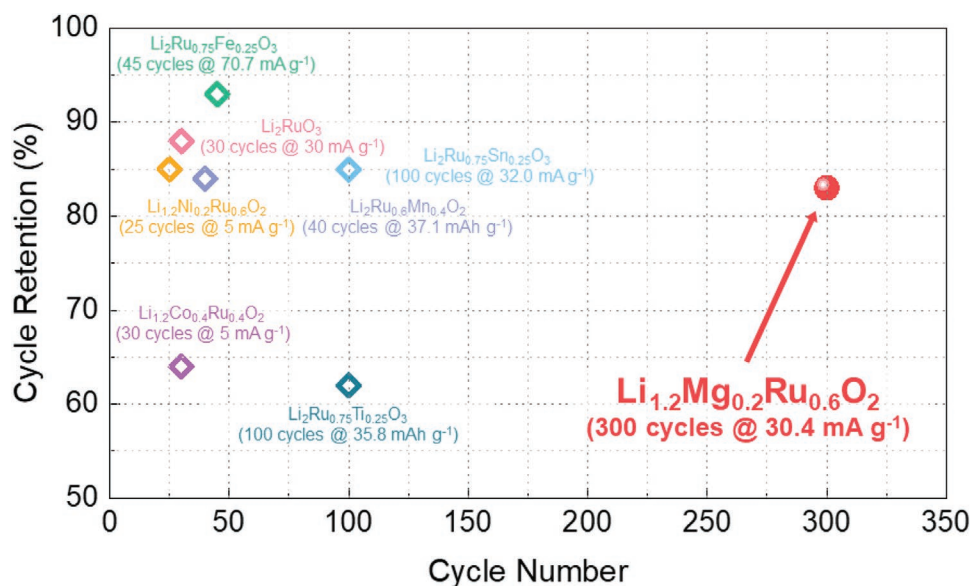


**Figure 6.** Comparison of the cycle performance of  $\text{Li}_{1.2}\text{Mg}_{0.2}\text{Ru}_{0.6}\text{O}_2$  and other Ru-based LRLOs.

theoretical activation barrier energies of  $\text{Li}^+$  diffusion in the  $\text{Li}_{1.2-x}\text{Mg}_{0.2}\text{Ru}_{0.6}\text{O}_2$  structure using the nudged elastic band method and first-principles calculations. When a  $\text{Li}^+$  ion moves through the diffusion path shown in Figure 5c, the predicted activation energy is 437 eV (Figure 5d). This value is comparable to the energy barrier of Li migration in  $\text{LiCoO}_2$ ,<sup>[44]</sup>  $\text{LiNi}_{0.5}\text{Mn}_{0.5}\text{O}_2$ ,<sup>[45]</sup> and  $\text{Li}[\text{Ni}_x\text{Co}_y\text{Mn}_{1-x-y}]\text{O}_2$ ,<sup>[46]</sup> theoretically supporting the high rate capability demonstrated here.

Furthermore,  $\text{Li}_{1.2}\text{Mg}_{0.2}\text{Ru}_{0.6}\text{O}_2$  retained 83% of the capacity after 300 cycles with a high Coulombic efficiency of over 99% (Figure 5e). The excellent cycle life originates from the highly reversible phase transition between two O3-type phases, avoiding the O3–O1 phase transition, as well as the strongly restricted cation migration, which results in deterioration of the structural and electrochemical reversibility. Because of the high structural stability and low strain, the active particles retained their original morphology and crystal structure even after 300 cycles (Figure S21, Supporting Information). In addition, the cyclability of  $\text{Li}_{1.2}\text{Mg}_{0.2}\text{Ru}_{0.6}\text{O}_2$  was enhanced compared with that of previously reported Ru-based LRLOs<sup>[11,12,26,47–50]</sup> (Figure 6), indicating that Mg substitution can play a key role in the structural stabilization and high electrochemical performance of LRLOs.

### 3. Conclusion

We showed that the substitution of redox-inactive  $\text{Mg}^{2+}$  in the LRLO structure can be used as an effective strategy to achieve excellent capacity and voltage retention while reversibly exploiting the cationic and anionic redox reactions. Using various structural probes, we demonstrated that unlike most LRLOs,  $\text{Li}_{1.2}\text{Mg}_{0.2}\text{Ru}_{0.6}\text{O}_2$  exhibits unprecedentedly high structural stability and suppressed structural disordering, with avoidance of cation migration and the O3–O1 phase transition. Even after numerous electrochemical cycles, Ru cations barely migrated

along the in-plane and out-of-plane directions. First-principles calculations revealed that the heterogenous local configuration near oxygen anions resulting from the Mg substitution induces the selective anionic redox reaction, leading to suppressed contraction of  $\text{RuO}_6$  octahedral sites. The spacious  $\text{RuO}_6$  octahedrons with less severe distortion enable the effective decoordination of the oxidized oxygen and the formation of short Ru–O bonds via a minor displacement of Ru within the original sites, forbidding the structural disordering. Given the high structural stability,  $\text{Li}_{1.2}\text{Mg}_{0.2}\text{Ru}_{0.6}\text{O}_2$  delivered a high reversible capacity of 283 mAh g<sup>-1</sup>, corresponding to 1.12 mol  $\text{Li}^+$  de/intercalation per formula unit, with retention of 83% of the initial capacity after 300 cycles.

Our discovery establishes the role of substituents with large ionic sizes and rigid O–M–O bond angles in stabilizing layered structures. Although further study is needed to confirm the effect of Mg substitution in 3d-TM-based LRLOs, we believe that our approach will be an effective strategy for the design of high-capacity LRLOs with improved structural, microstructural, and electrochemical stability through control of the local atomic configurations and oxygen electronic structure.

### 4. Experimental Section

**Synthesis of  $\text{Li}_{1.2}\text{Mg}_{0.2}\text{Ru}_{0.6}\text{O}_2$  and  $\text{Li}_2\text{RuO}_3$ :** The materials were prepared using a simple solid-state method.  $\text{Li}_2\text{CO}_3$  (Sigma Aldrich, 99.99%),  $\text{Mg}(\text{NO}_3)_2 \cdot 6\text{H}_2\text{O}$  (Samchun Chemical, 98%), and  $\text{RuO}_2$  (Alfa Aesar, 99%) were used as precursors. Stoichiometric amounts of the precursors were mixed using high-energy ball milling at 400 rpm for 3 h. After mixing, the obtained powder was pelletized and calcined under 0.3 L min<sup>-1</sup> flow of dried air gas in an alumina crucible.  $\text{Li}_{1.2}\text{Mg}_{0.2}\text{Ru}_{0.6}\text{O}_2$  and  $\text{Li}_2\text{RuO}_3$  were calcined at 950 °C for 15 h.

**X-Ray Diffraction:**  $\text{Li}_{1.2}\text{Mg}_{0.2}\text{Ru}_{0.6}\text{O}_2$  and  $\text{Li}_2\text{RuO}_3$  were analyzed using an X-ray diffractometer (PANalytical Empyrean) with Cu K $\alpha$  radiation ( $\lambda = 1.54178 \text{ \AA}$ ) in the  $2\theta$  range of 10° to 80° with a step size of 0.013°. Rietveld refinement of the XRD data was performed using FullProf software.<sup>[51]</sup> Operando XRD (o-XRD) patterns were obtained during

charge/discharge at a current density of 30.4 mA g<sup>-1</sup> within the voltage range of 2.0–4.4 V (vs Li<sup>+</sup>/Li). Operando XRD patterns of Li<sub>2</sub>RuO<sub>3</sub> were obtained using an X-ray diffractometer (PANalytical Empyrean) with Cu K $\alpha$  radiation ( $\lambda = 1.54178 \text{ \AA}$ ) in the  $2\theta$  range of 16° to 60° with a step size of 0.013°. An operando XRD battery cell (ISBC) made by PANalytical with PDF TECH was used for the operando XRD experiments. In addition, Li<sub>1.2</sub>Mg<sub>0.2</sub>Ru<sub>0.6</sub>O<sub>2</sub> operando synchrotron XRD ( $\alpha$ -SXRD) patterns were obtained at the 3D XRS beamline at the Pohang Accelerator Laboratory (PAL), South Korea, using synchrotron radiation ( $\lambda = 0.688725 \text{ \AA}$ ) with a Mar345 image plate detector in transmission mode and an X-ray exposure time of 5 s. After the measurement, the  $2\theta$  angles of all the  $\alpha$ -SXRD patterns were converted into the corresponding angles for  $\lambda = 1.54178 \text{ \AA}$  (the wavelength of a conventional X-ray tube source with Cu K $\alpha$  radiation) for ease of comparison with other studies.

**Inductively Coupled Plasma Atomic Emission Spectroscopy:** The atomic ratio of elements such as Li, Mg, and Ru was determined using an inductively coupled plasma emission spectrometer (ICP-AES; OPTIMA 8300, Perkin-Elmer).

**Scanning Electron Microscopy:** The morphology of the materials was determined using FE-SEM (SU-8010, HITACHI) at 15 keV. All the samples were coated with Pt nanoparticles to enhance the conductivity.

**Transmission Electron Microscopy:** High-resolution TEM (HR-TEM) particle images, atomic-resolution STEM-HAADF images, SAED patterns and the d-spacing, and EDS elemental maps were obtained using a Cs-corrected microscope (FEI, TITAN TM 80–300) operated at 300 keV. The available point resolution was better than 1 Å at the operating accelerating voltage. Each image was recorded by a 4k  $\times$  4k CCD camera (Gatan Oneview 1095). Before the measurements, each sample was dispersed in ethanol using an ultrasonicator, and a drop of the suspension was sprayed onto a carbon-coated Cu TEM grid, which was dried at room temperature overnight to evaporate the ethanol.

**X-Ray Absorption Spectroscopy:** Ex situ XAS spectra for the Ru K-edge were obtained at the 10 C Wide XAFS beamline at Pohang Accelerator Laboratory (PAL). Ru K-edge spectra were collected in transmission mode with an energy range of 21 917–23 088 eV including the XANES and EXAFS regions, and Ru reference spectra were simultaneously obtained from Ru metal foil. sXAS spectra for the O K-edge were measured in high-energy grating (HEG) with a photon energy range of 525–560 eV at the 4D PES beamline at PAL. The collected XAS and sXAS data were analyzed using Athena software.<sup>[52]</sup> Each sample was prepared in the form of an electrode.

**Electrochemical Characterization:** The Li<sub>1.2</sub>Mg<sub>0.2</sub>Ru<sub>0.6</sub>O<sub>2</sub> and Li<sub>2</sub>RuO<sub>3</sub> electrodes were fabricated by mixing 70 wt% active material, 20 wt% Super P carbon black, and 10 wt% polyvinylidene fluoride (PVDF) using *N*-methyl-2-pyrrolidone (NMP) as the solvent. The slurry was cast on Al foil and dried at 100 °C overnight under the vacuum condition. After drying, the electrode was punched into a disk of 10 $\pi$  mm diameter. The mass loading of the electrode was  $\approx 2 \text{ mg cm}^{-2}$ . CR2032-type coin cells were assembled as half-cells using Li metal as the counter electrode, a separator (Celgard 2400), and 1.2 M LiPF<sub>6</sub> in ethylene carbonate (EC):dimethyl carbonate (DMC) = 3:7 v/v as the electrolyte. The coin cells were assembled in an Ar-filled glove box. Galvanostatic charge/discharge tests were performed at various current densities (15.2, 30.4, 60.8, 152, 304, and 608 mA g<sup>-1</sup> in the voltage range of 2.0–4.4 V (vs Li<sup>+</sup>/Li); the charge current density was fixed at 15.2 mA g<sup>-1</sup>) using an automatic battery charge/discharge test system (WBCS 3000, WonATech). The cycle performance was measured after the first charge/discharge at a current density of 15.2 mA g<sup>-1</sup>. In addition, GITT measurement of the electrodes was performed at a current density of 15.2 mA g<sup>-1</sup> with 30 min charge/discharge and 10 min relaxation for each step.

**In Situ Differential Electrochemical Mass Spectroscopy:** The mass spectroscopy (Hiden Analytical, UK) was used to detect the amounts of O<sub>2</sub> and CO<sub>2</sub> gases that evolved during the electrochemical test. Coin cells with a hole in case were used for DEMS test and inserted into DEMS cell enabling gas flow in and flow out. Each cell was connected to the DEMS analysis line, which comprised Ar carrier gas, a mass flow controller, an inlet/outlet gas line for cell connection, and a mass spectrometer. Ar gas (99.999%) was used as the carrier gas, and the flow was adjusted to

2.5 mL min<sup>-1</sup>. The inner space of the cell was washed out with Ar gas to remove residual impurities, and after flushing, the cell was charged/discharged at a current density of 30.4 mA g<sup>-1</sup> in the voltage range of 2.0–4.4 V.

**Computational Details:** All the DFT calculations were performed using the Vienna Ab initio Simulation Package (VASP).<sup>[53]</sup> Projector-augmented wave pseudopotentials were used with a plane-wave basis set, as implemented in VASP.<sup>[54]</sup> Perdew–Burke–Ernzerhof parametrization of the generalized gradient approximation<sup>[55]</sup> was used for the exchange–correlation functional. For the DFT calculations, a 6  $\times$  6  $\times$  2 k-point grid was used to calculate a 1  $\times$  1  $\times$  1 supercell structure of Li<sub>1.2</sub>Mg<sub>0.2</sub>Ru<sub>0.6</sub>O<sub>2</sub>. The GGA+U method was adopted to address the localization of the d-orbital in Ru ions, with a *U* value of 4.0 eV, as used in a previous study.<sup>[40]</sup> The Heyd–Scuseria–Ernzerhof (HSE06) hybrid functional was applied to accurately calculate the pDOS of O and Ru.<sup>[40,56]</sup> A kinetic energy cutoff of 500 eV was used in all the calculations, and all the structures were optimized until the force in the unit cell converged to within 0.03 eV Å<sup>-1</sup>. CASM<sup>[17]</sup> software was used to generate all the Li/vacancy configurations for each composition, followed by filling DFT calculations on a maximum of 20 configurations with the lowest electrostatic energy for each composition used to obtain the convex hull of Li<sub>1.2</sub>Mg<sub>0.2</sub>Ru<sub>0.6</sub>O<sub>2</sub>.

## Supporting Information

Supporting Information is available from the Wiley Online Library or from the author.

## Acknowledgements

J.A. and J.K. contributed equally to this work. This work was supported by the National Research Foundation of Korea (NRF) grant funded by the Korea government (MSIT) (2021R1A2C1014280, 2021R1C1C1006721, 2020M2D8A2070870, 2020M3H4A1A03084256, and 2021M3H4A1A01079215). Also, this work was supported by the institutional program of the Korea Institute of Science and Technology (KIST, Project no. 2E30993).

## Conflict of Interest

The authors declare no conflict of interest.

## Data Availability Statement

Data available on request from the authors.

## Keywords

anionic redox, cation migration, first-principles calculations, high energy density, Li-ion batteries, Li-rich layered oxides

Received: July 28, 2021  
Revised: September 28, 2021  
Published online: October 28, 2021

- [1] J. Lee, N. Dupre, M. Jeong, S. Y. Kang, M. Avdeev, Y. Gong, L. Gu, W. S. Yoon, B. Kang, *Adv. Sci.* **2020**, *7*, 2001658.
- [2] M. Saubanère, E. McCalla, J. M. Tarascon, M. L. Doublet, *Energy Environ. Sci.* **2016**, *9*, 984.
- [3] A. Grimaud, W. T. Hong, Y. Shao-Horn, J. M. Tarascon, *Nat. Mater.* **2016**, *15*, 121.

- [4] J. Wang, X. He, E. Paillard, N. Laszczynski, J. Li, S. Passerini, *Adv. Energy Mater.* **2016**, *6*, 1600906.
- [5] J. H. Kim, K. J. Park, S. J. Kim, C. S. Yoon, Y. K. Sun, *J. Mater. Chem. A* **2019**, *7*, 2694.
- [6] W. Zhao, W. Choi, W. S. Yoon, *J. Electrochem. Sci. Technol.* **2020**, *11*, 195.
- [7] E. McCalla, A. M. Abakumov, M. Saubanere, D. Foix, E. J. Berg, G. Rousse, M.-L. Doublet, D. Gonbeau, P. Novak, G. Van Tendeloo, R. Dominko, J.-M. Tarascon, *Science* **2015**, *350*, 1516.
- [8] P. E. Pearce, A. J. Perez, G. Rousse, M. Saubanère, D. Batuk, D. Foix, E. McCalla, A. M. Abakumov, G. Van Tendeloo, M. L. Doublet, J. M. Tarascon, *Nat. Mater.* **2017**, *16*, 580.
- [9] M. Okubo, A. Yamada, *ACS Appl. Mater. Interfaces* **2017**, *9*, 36463.
- [10] F. Ning, B. Li, J. Song, Y. Zuo, H. Shang, Z. Zhao, Z. Yu, W. Chu, K. Zhang, G. Feng, X. Wang, D. Xia, *Nat. Commun.* **2020**, *11*, 4973.
- [11] M. Sathiya, A. M. Abakumov, D. Foix, G. Rousse, K. Ramesha, M. Saubanère, M. L. Doublet, H. Vezin, C. P. Laisa, A. S. Prakash, D. Gonbeau, G. Vantendeloo, J. M. Tarascon, *Nat. Mater.* **2015**, *14*, 230.
- [12] M. Sathiya, K. Ramesha, G. Rousse, D. Foix, D. Gonbeau, S. Prakash, M. L. Doublet, K. Hemalatha, J.-M. Tarascon, *Chem. Mater.* **2013**, *25*, 1121.
- [13] W. E. Gent, I. I. Abate, W. Yang, L. F. Nazar, W. C. Chueh, *Joule* **2020**, *4*, 1369.
- [14] J. Hong, W. E. Gent, P. Xiao, K. Lim, D. H. Seo, J. Wu, P. M. Csernica, C. J. Takacs, D. Nordlund, C. J. Sun, K. H. Stone, D. Passarello, W. Yang, D. Prendergast, G. Ceder, M. F. Toney, W. C. Chueh, *Nat. Mater.* **2019**, *18*, 256.
- [15] W. E. Gent, K. Lim, Y. Liang, Q. Li, T. Barnes, S. J. Ahn, K. H. Stone, M. McIntire, J. Hong, J. H. Song, Y. Li, A. Mehta, S. Ermon, T. Tyliczszak, D. Kilcoyne, D. Vine, J. H. Park, S. K. Doo, M. F. Toney, W. Yang, D. Prendergast, W. C. Chueh, *Nat. Commun.* **2017**, *8*, 2091.
- [16] R. A. House, U. Maitra, M. A. Pérez-Osorio, J. G. Lozano, L. Jin, J. W. Somerville, L. C. Duda, A. Nag, A. Walters, K. J. Zhou, M. R. Roberts, P. G. Bruce, *Nature* **2020**, *577*, 502.
- [17] A. Van der Ven, J. C. Thomas, Q. Xu, J. Bhattacharya, *Math. Comput. Simul.* **2010**, *80*, 1393.
- [18] J. Xu, M. Sun, R. Qiao, S. E. Renfrew, L. Ma, T. Wu, S. Hwang, D. Nordlund, D. Su, K. Amine, J. Lu, B. D. McCloskey, W. Yang, W. Tong, *Nat. Commun.* **2018**, *9*, 947.
- [19] Y. Yu, P. Karayaylali, D. Sokaras, L. Giordano, R. Kou, C. J. Sun, F. Maglia, R. Jung, F. S. Gittleson, Y. Shao-Horn, *Energy Environ. Sci.* **2021**, *14*, 2322.
- [20] K. Xu, *Chem. Rev.* **2004**, *104*, 4303.
- [21] S. Tan, Y. J. Ji, Z. R. Zhang, Y. Yang, *ChemPhysChem* **2014**, *15*, 1956.
- [22] D. Aurbach, B. Markovsky, G. Salitra, E. Markevich, Y. Talyossef, M. Koltypin, L. Nazar, B. Ellis, D. Kovacheva, *J. Power Sources* **2007**, *165*, 491.
- [23] K. Ku, J. Hong, H. Kim, H. Park, W. M. Seong, S. K. Jung, G. Yoon, K. Y. Park, H. Kim, K. Kang, *Adv. Energy Mater.* **2018**, *8*, 1800606.
- [24] G. Assat, C. Delacourt, D. A. D. Corte, J.-M. Tarascon, *J. Electrochem. Soc.* **2016**, *163*, A2965.
- [25] H. Jang, W. Jin, G. Nam, Y. Yoo, J. S. Jeon, J. Park, M. G. Kim, J. Cho, *Energy Environ. Sci.* **2020**, *13*, 2167.
- [26] M. Sathiya, G. Rousse, K. Ramesha, C. P. Laisa, H. Vezin, M. T. Sougrati, M. L. Doublet, D. Foix, D. Gonbeau, W. Walker, A. S. Prakash, M. Ben Hassine, L. Dupont, J. M. Tarascon, *Nat. Mater.* **2013**, *12*, 827.
- [27] J. Hong, D. H. Seo, S. W. Kim, H. Gwon, S. T. Oh, K. Kang, *J. Mater. Chem.* **2010**, *20*, 10179.
- [28] J. Zheng, S. Myeong, W. Cho, P. Yan, J. Xiao, C. Wang, J. Cho, J. G. Zhang, *Adv. Energy Mater.* **2017**, *7*, 1601284.
- [29] H. Kobayashi, *Solid State Ionics* **1995**, *82*, 25.
- [30] P. Muhammed Shafi, A. Chandra Bose, *AIP Adv.* **2015**, *5*, 057137.
- [31] K. Venkateswarlu, A. Chandra Bose, N. Rameshbabu, *Phys. B* **2010**, *405*, 4256.
- [32] B. B. He, *Two-Dimensional X-Ray Diffraction*, John Wiley & Sons, Inc., Hoboken, NJ **2018**.
- [33] D. N. Mueller, M. L. MacHala, H. Bluhm, W. C. Chueh, *Nat. Commun.* **2015**, *6*, 6097.
- [34] W. S. Yoon, M. Balasubramanian, K. Y. Chung, X. Q. Yang, J. McBreen, C. P. Grey, D. A. Fischer, *J. Am. Chem. Soc.* **2005**, *127*, 17479.
- [35] M. Abbate, F. M. F. De Groot, J. C. Fuggle, A. Fujimori, O. Strebel, M. F. Lopez, M. Domke, G. Kaindl, G. A. Sawatzky, M. Takano, Y. Takeda, H. Eisaki, S. Uchida, *Phys. Rev. B* **1992**, *46*, 4511.
- [36] R. A. House, L. Jin, U. Maitra, K. Tsuruta, J. W. Somerville, D. P. Förstermann, F. Massel, L. Duda, M. R. Roberts, P. G. Bruce, *Energy Environ. Sci.* **2018**, *11*, 926.
- [37] D. Eum, B. Kim, S. J. Kim, H. Park, J. Wu, S. P. Cho, G. Yoon, M. H. Lee, S. K. Jung, W. Yang, W. M. Seong, K. Ku, O. Tamwattana, S. K. Park, I. Hwang, K. Kang, *Nat. Mater.* **2020**, *19*, 419.
- [38] G. Assat, A. Iadecola, D. Foix, R. Dedryvere, J. M. Tarascon, *ACS Energy Lett.* **2018**, *3*, 2721.
- [39] E. Hu, Q. Li, X. Wang, F. Meng, J. Liu, J. N. Zhang, K. Page, W. Xu, L. Gu, R. Xiao, H. Li, X. Huang, L. Chen, W. Yang, X. Yu, X. Q. Yang, *Joule* **2021**, *5*, 720.
- [40] D. H. Seo, J. Lee, A. Urban, R. Malik, S. Kang, G. Ceder, *Nat. Chem.* **2016**, *8*, 692.
- [41] K. Ku, B. Kim, S. K. Jung, Y. Gong, D. Eum, G. Yoon, K. Y. Park, J. Hong, S. P. Cho, D. H. Kim, H. Kim, E. Jeong, L. Gu, K. Kang, *Energy Environ. Sci.* **2020**, *13*, 1269.
- [42] E. McCalla, M. T. Sougrati, G. Rousse, E. J. Berg, A. Abakumov, N. Recham, K. Ramesha, M. Sathiya, R. Dominko, G. Van Tendeloo, P. Novák, J. M. Tarascon, *J. Am. Chem. Soc.* **2015**, *137*, 4804.
- [43] J. Ma, Y. N. Zhou, Y. Gao, X. Yu, Q. Kong, L. Gu, Z. Wang, X. Q. Yang, L. Chen, *Chem. Mater.* **2014**, *26*, 3256.
- [44] A. Van Der Ven, G. Ceder, *Electrochem. Solid-State Lett.* **2000**, *3*, 301.
- [45] K. Kang, *Science* **2006**, *311*, 977.
- [46] Y. Wei, J. Zheng, S. Cui, X. Song, Y. Su, W. Deng, Z. Wu, X. Wang, W. Wang, M. Rao, Y. Lin, C. Wang, K. Amine, F. Pan, *J. Am. Chem. Soc.* **2015**, *137*, 8364.
- [47] N. Li, S. Hwang, M. Sun, Y. Fu, V. S. Battaglia, D. Su, W. Tong, *Adv. Energy Mater.* **2019**, *9*, 1902258.
- [48] N. Li, J. Wu, S. Hwang, J. K. Papp, W. H. Kan, L. Zhang, C. Zhu, B. D. McCloskey, W. Yang, W. Tong, *ACS Energy Lett.* **2020**, *5*, 3535.
- [49] R. Satish, K. Lim, N. Bucher, S. Hartung, V. Aravindan, J. Franklin, J. S. Lee, M. F. Toney, S. Madhavi, *J. Mater. Chem. A* **2017**, *5*, 14387.
- [50] B. Li, R. Shao, H. Yan, L. An, B. Zhang, H. Wei, J. Ma, D. Xia, X. Han, *Adv. Funct. Mater.* **2016**, *26*, 1330.
- [51] J. Rodríguez-Carvajal, *Comm. Powder Diffr. (IUCr). Newsl.* **2001**, *26*, 12.
- [52] B. Ravel, M. Newville, *Phys. Scr., T* **2005**, *T115*, 1007.
- [53] G. Kresse, J. Furthmüller, *Comput. Mater. Sci.* **1996**, *6*, 15.
- [54] P. E. Blöchl, *Phys. Rev. B* **1994**, *50*, 17953.
- [55] J. P. Perdew, K. Burke, M. Ernzerhof, *Phys. Rev. Lett.* **1996**, *77*, 3865.
- [56] J. Heyd, G. E. Scuseria, M. Ernzerhof, *J. Chem. Phys.* **2003**, *118*, 8207.